

***In vivo* continuous-wave optical breast imaging enhanced with Indocyanine Green**

Xavier Intes^{a)}

*Department of Biochemistry and Biophysics and Department of Physics and Astronomy,
University of Pennsylvania, Philadelphia, Pennsylvania 19104*

Jorge Ripoll

Institute of Electronic Structure and Laser, FORTH, Crete

Yu Chen and Shoko Nioka

Department of Biochemistry and Biophysics, University of Pennsylvania, Philadelphia, Pennsylvania 19104

A. G. Yodh

Department of Physics and Astronomy, University of Pennsylvania, Philadelphia, Pennsylvania 19104

Britton Chance

Department of Biochemistry and Biophysics, University of Pennsylvania, Philadelphia, Pennsylvania 19104

(Received 20 November 2002; revised 4 February 2003; accepted for publication 24 March 2003; published 23 May 2003)

We investigate the uptake of a nontargeted contrast agent by breast tumors using a continuous wave diffuse optical tomography apparatus. The instrument operates in the near-infrared spectral window and employs 16 sources and 16 detectors to collect light in parallel on the surface of the tumor-bearing breast (coronal geometry). In our protocol an extrinsic contrast agent, Indocyanine Green (ICG), was injected by bolus. Three clinical scenarios with three different pathologies were investigated. A two-compartment model was used to analyze the pharmacokinetics of ICG and preprocess the data, and diffuse optical tomography was used for imaging. Localization and delineation of the tumor was achieved in good agreement with *a priori* information. Moreover, different dynamical features were observed for differing pathologies. The malignant cases exhibited slower rate constants (uptake and outflow) compared to healthy tissue. These results provide further evidence that *in vivo* pharmacokinetics of ICG in breast tumors may be a useful diagnostic tool for differentiation of benign and malignant pathologies. © 2003 American Association of Physicists in Medicine. [DOI: 10.1118/1.1573791]

Key words: tomography, mammography, photon migration, photon density waves, contrast agent

I. INTRODUCTION

Light has been used for centuries as a means to probe human tissue. However, in the last decade the near-infrared (NIR) spectral window has received special interest. In this spectral range, human tissues are characterized by relatively low absorption and relatively high scattering. Thus NIR light diffuses through most tissues. The chromophore accountable for most NIR absorption is hemoglobin in its different forms. As a result, NIR optical techniques provide a method to investigate deep tissues and reveal functional information about these tissues, with the advantage of low power and noninvasiveness.

A wide range of biomedical applications may benefit from these recent developments, for example cancer detection and characterization. By probing local blood concentration and oxygenation, the NIR techniques provide insight about cancer physiology. Preliminary clinical data has already reported breast cancer detection and characterization.¹⁻⁵ However, it is sometimes difficult to assess the significance of the absorption-derived intrinsic parameters because of other tissue optical-variations due to hormonal status.⁶⁻⁸ In addition, thus far the scattering coefficient appears to be a nonreliable

diagnostic parameter.^{9,10} It is therefore still desirable to investigate alternative NIR diagnostic tools with potentially higher tissue/tumor contrast.

Extrinsic contrast agents play a critical role in magnetic resonance imaging (MRI)¹¹ and positron emission tomography (PET).¹² Similarly, we anticipate contrast agents in the NIR will provide added diagnostic information for DOT,^{13,14} especially as new generations of contrast agents are designed to target molecular and genetic expression of tumors.¹⁵⁻¹⁸ Presently, however, these extrinsic compounds are not available for human studies. To assess the potential of contrast agents in clinical trials, one must use FDA approved compounds. Indocyanine Green (ICG) meets most needs for optical techniques. The compound is safe, it is approved by US Food and Drug Administration, and is commonly used clinically for diagnostic purposes.¹⁹⁻²¹ Moreover, it possesses an absorption and fluorescence spectra in the NIR window.²² NIR studies using ICG in breast cancer detection have already been reported.^{13,23} Studies in tissue phantoms,^{24,25} in animal models^{26,27} and in humans^{28,29} have demonstrated its potential uses and its ability to enhance tumor-to-healthy-tissue contrast. Principally as a result of its high binding

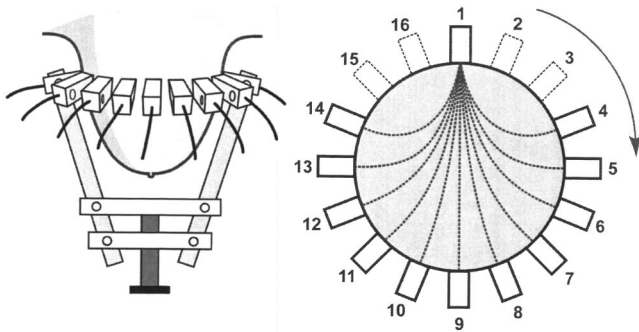


FIG. 1. CW imager configuration. The sources are sequentially shining upon the breast and so the configuration is equivalent to a fan-beam configuration.

percentage to blood proteins, ICG is a blood pooling agent providing sensitivity to hyper-vascularization. Its distribution is mainly intravascular; extravasation is likely to occur only in the highly permeable blood capillaries of tumors.³⁰

In this work we explore the *in vivo* uptake dynamics of ICG in breast tumors using a continuous wave (CW) NIR imaging apparatus. Three patients with suspicious masses were enrolled for this first trial. In each case, localization and delineation of the tumor was achieved in good agreement with *a priori* information. Furthermore, different dynamical behaviors were observed, and were found to be correlated with three different pathologies determined afterwards by biopsy. Malignant tumors exhibited slower rate constants (uptake and outflow) compared to healthy tissue. Conversely the benign case exhibited similar rate constants.

The structure of this article is as follows. First we introduce the methods employed, including a brief introduction to the apparatus, a presentation of the pharmacokinetic model, and a description of the inverse problem. Second, we present reconstructions obtained from a tissue phantom and from the three *in vivo* cases. *In vivo* pharmacokinetics are derived using these reconstructions. Discussion of these results is followed by a brief conclusion.

II. METHODS

A. Apparatus

The system used in this study has been described in detail elsewhere.²⁸ The current design is given in Fig. 1. Briefly, the system employs 16 light sources (derived from a tungsten bulb) located on a circular holder. Sixteen detectors (silicon photodiodes) are situated in the same plane and use the same positions as the sources to collect (in parallel) the light originating from one source at a time. A band pass filter (typically at 805 ± 20 nm) is placed in front of the source to select the incident wavelength.

The breast is arranged in a pendular geometry with the source-detector probes gently touching its surface (cf. Fig. 1). A set of data for one source is collected every 500 ms. The total time for a whole scan of the breast (16 sources \times 16 detectors) is ≈ 8 s. Due to the large dynamic range in the data, only signals from the farthest 11 detectors are used in the analysis, i.e., detectors drawn with plain lines in Fig. 1.

B. Protocol

Patients with suspicious masses were enrolled for this study. Measurements were made prior to biopsy to avoid modification of the blood volume and blood flow in the tumor area. *A priori* knowledge on the location and size of the tumor was derived by palpation. This information was used to position the probe holding sources and detectors in the coronal plane bearing the tumor. Diagnostic information was obtained *a posteriori* from biopsy and eventually surgery.

ICG was injected intravenously by bolus with a concentration of 0.25 mg per kg of body weight. Data acquisition from the apparatus were derived shortly before the injection and continued for the next 10 min.

C. Pharmacokinetics

ICG has been used for 40 years in different areas of medicine. Its metabolic and physiological features are well documented.²² The spectral properties of ICG are suitable for NIR applications. The maximum absorption occurs at 805 nm in whole blood and its fluorescence peaks at 830 nm. The molecule is amphiphilic and exhibits a strong affinity to blood proteins. Therefore, the distribution of ICG is expected to be mainly intravascular. Researchers are using this property to delineate tumor tissues.³¹ Although extravasation of the molecule has been reported in some tumor lines, extravasation is not expected to be universal.³⁰

The compound is extracted from the blood by the hepatocytes and clears from the blood in several minutes. Two-compartment models have been predominantly used to analyze the pharmacokinetics of the ICG.^{32,33} We use the approach of Shinohara *et al.*:

$$\text{ICG}(t) = -A \exp(-\alpha t) + B \exp(-\beta t), \quad (1)$$

where $\text{ICG}(t)$ is the time dependent concentration curve following the injection, and α and β [min^{-1}] are the rate constants for ICG uptake and release, respectively. A and B determine the zero time intercepts. This model is used to follow the global (one source-detector pair) and the local (one voxel in the image reconstructions) pharmacokinetics of ICG. The pharmacokinetics of ICG were used as part of the *a priori* information set to select the optimum configuration for DOT.

Raw data were fitted to Eq. (1) using a standard nonlinear Nelder–Mead simplex search.³⁴ Goodness of the fit was assessed by the R^2 value. Raw intensity data leading to a fit with $R^2 \leq 0.75$ were disregarded from consideration in the reconstruction algorithm. The rationale of this preprocessing of the data is linked to biological noise we noticed in our measurements; biological noise can hamper our ability to obtain accurate reconstructions.

D. The analytical forward model

Propagation of light in soft human tissue such as breast is modeled by the diffusion approximation.³⁵ This model provides a framework for consideration of inhomogeneities em-

bedded in tissues, such as tumors. The heterogeneous diffusion equation we use to model our problem (with scattering assumed constant and homogeneous) is

$$[\nabla^2 + k^2 + O(\vec{r})]U(\vec{r}, \vec{r}_s) = -AS(\vec{r}_s)/D. \quad (2)$$

Here $U(\vec{r}, \vec{r}_s)$ is the fluence rate ($\text{W}\cdot\text{cm}^{-2}$) (isotropic term), $D = (3\mu'_s)^{-1}$ is the light diffusion coefficient in cm, μ_a is the absorption coefficient (cm^{-1}), μ'_s the reduced scattering coefficient (cm^{-1}), and $AS(\vec{r}_s)$ the source term. Here k is a wavenumber obeying the relation, $k^2 = -v\mu_a - i\omega/vD$ (ω = angular modulation frequency set to zero in our case; v = light speed in media), and $O(\vec{r})$ represents the heterogeneity operator, i.e.,

$$O(\vec{r}) = \frac{v\Delta\mu_a(\vec{r})}{D}. \quad (3)$$

Analytical solutions of this equation are derived using perturbative approaches. In our case, we used the first-order Rytov approximation. The sample volume is divided into a set of voxels and the measurements are related to the unknowns (in this case relative absorption coefficient) of each voxel by a system of linear equations:

$$\begin{bmatrix} \Phi_{sc}(\vec{r}_{s1}, \vec{r}_{d1}) \\ \vdots \\ \Phi_{sc}(\vec{r}_{sm}, \vec{r}_{dm}) \end{bmatrix} = \begin{bmatrix} W_{11} & \dots & W_{1n} \\ \vdots & \ddots & \vdots \\ W_{m1} & \dots & W_{mn} \end{bmatrix} \begin{bmatrix} \Delta\mu_a(\vec{r}_1) \\ \vdots \\ \Delta\mu_a(\vec{r}_n) \end{bmatrix}. \quad (4)$$

Here $\Phi_{sc}(\vec{r}_s, \vec{r}_d) = -\ln[U_{\text{post-injection}}(\vec{r}_s, \vec{r}_d)/U_{\text{pre-injection}}(\vec{r}_s, \vec{r}_d)]$ is the diffuse Rytov perturbative phase for the i th source-detector pair, W_{ij} is the weight function for the j th voxel and the i th source-detector pair, and $\Delta\mu_a(\vec{r}_j)$ is the differential absorption coefficient of the j th voxel. The derivation and the expression of the weight function can be found in the thesis by O'Leary³⁶ and a detailed description of the differential formulation based on postinjection/preinjection has been described by Ntziachristos *et al.*³⁷

The shape of the breast was approximated as a cylinder (cf. Fig. 2), and the Kirchhoff approximation (KA)^{38,39} for diffusive waves was used to model the interaction of light with the boundaries. For the cases presented here, the KA had less than a 1% deviation from the rigorous solution to the diffusion equation.

In order to account for biological noise (e.g., breathing motions), the forward model was implemented with the coupling coefficient technique.⁴⁰ This approach compensates for variations of detected intensity light due to perturbations created at the source or the detector by biological noise. For this purpose, the object function (formally the vector of absorption heterogeneity) was augmented:

$$x = \left[\frac{\Delta\mu_a(\vec{r}_1)}{\mu_{a0}} \dots \frac{\Delta\mu_a(\vec{r}_n)}{\mu_{a0}} \ln s_1 \dots \ln s_{N_s} \ln d_1 \dots \ln d_{N_d} \right]. \quad (5)$$

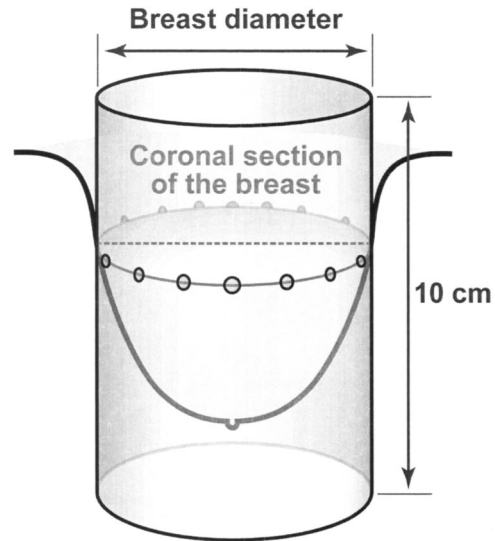


FIG. 2. Boundary condition model.

Here s_k stands for the source-coupling amplitudes and d_k for the detector-coupling amplitudes. The reader is encouraged to read Ref. 40 for an in-depth derivation of the theoretical technique.

E. The inverse problem

The inverse problem can be addressed by various schemes.⁴¹ In this study, we chose the singular value decomposition (SVD) of the Moore–Penrose generalized system:

$$x_{\text{est}} = W^T \cdot (W \cdot W^T + \lambda \cdot I)^{-1} \cdot \Phi_{sc}, \quad (6)$$

where x_{est} is the object function vector, Φ_{sc} is the measurement vector, W^T is the transpose of the weight matrix, and $\lambda \cdot I$ is the regularization matrix. Tikhonov regularization was used to stabilize the inversion procedure.

The optimum regularization parameter was chosen by means of an L-curve analysis.⁴² The L-curve method was applied to an experimental model reconstruction and the best regularization parameter was derived using the curvature function, $K(\lambda)$, which was employed in the approach of Hansen *et al.*⁴³

$$K(\lambda) = \frac{\xi''(\lambda)\eta'(\lambda) - \xi'(\lambda)\eta''(\lambda)}{(\xi'(\lambda)^2 + \eta'(\lambda)^2)^{3/2}}, \quad (7)$$

where $\xi(\lambda) = \ln\|W \cdot x_{\text{est}} - \Phi_{sc}\|$ and $\eta(\lambda) = \ln\|x_{\text{est}}\|$ for a given regularization value λ . The superscripts ' and '' denote, respectively, the first and second derivatives with respect to λ . The best regularization parameter, corresponding to the minimum of the curvature function $K(\lambda)$, was derived from our experimental model, and was employed for all the reconstructions herein.

III. RESULTS

A. Tissue phantom

The reconstruction algorithm was characterized using a model system previously employed to validate the apparatus

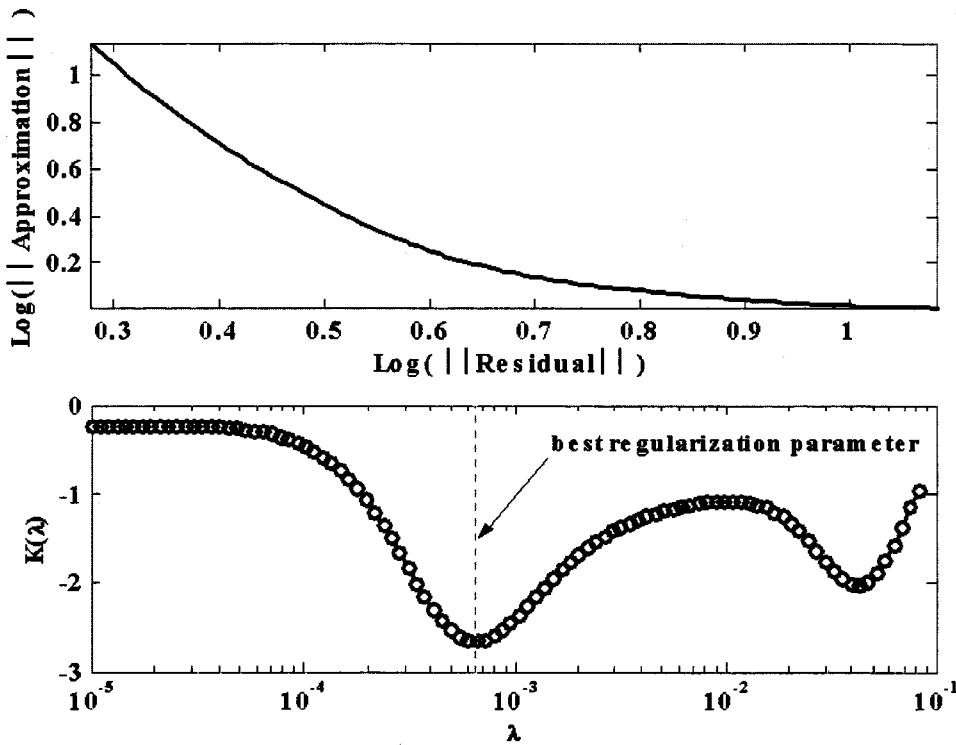


FIG. 3. L-curve analysis from the model experiment. The best regularization parameter was derived from this analysis.

potential.²⁸ This experimental sample consisted of an object embedded in an otherwise homogeneous medium with cylindrical boundary conditions (diameter=10 cm). The background media was created by a mixture of Intralipid and ink to obtain optical parameters mimicking breast tissue⁴⁸ ($\mu_a = 0.04 \text{ cm}^{-1}$ and $\mu'_s = 8 \text{ cm}^{-1}$). The contrast of the object was doubled during the experiment from $\Delta\mu_a = 0.03 \text{ cm}^{-1}$ to $\Delta\mu_a = 0.06 \text{ cm}^{-1}$. The object was a 2 cm diameter cylinder.

Our Tikhonov regularization constant is derived from this control experiment. Figure 3 presents the L-curve analysis and the curvature function associated with the differential absorption reconstructions. From the L-curve analysis described previously, the optimum regularization parameter was set to $\lambda = 6 \times 10^{-4}$ of the maximum eigenvalue of WW^T [see Eq. (6)]. Reconstructions from this experiment based on the optimum regularization parameter are presented in Fig. 4.

B. Clinical results

1. Case I: Fibroadenoma

This case corresponds to a mass estimated to be 1–2 cm in diameter by palpation within a breast of 9 cm diameter. The mass was located around 6–7 o'clock in the breast, relative to our angle representation herein, and near the skin surface (i.e., within ≈ 1 cm). The tumor was found to be a fibroadenoma by biopsy.

An example of the intensity trace collected by one detector for a particular source is displayed in Fig. 5 (source 14 and detector 4). The differential absorption reconstructions using the selected time represented by dots in Fig. 5 are presented in Fig. 6. The reference state was chosen before the injection of ICG as described in Sec. IID.

The reconstructions exhibit a maximum of uptake between 6 and 7 o'clock close to the surface. This maximum uptake corresponded to $\Delta\mu_a = 0.018 \text{ cm}^{-1}$. The location corresponds to the expected location of the tumor. From the maximum of uptake, the FWHM of the reconstructed inhomogeneity is estimated to $1.8 \text{ cm} \times 1.4 \text{ cm}$. Some artifacts were also noticeable close to the location of the heterogeneity, though they had lower magnitudes and different time behaviors.

2. Case II: Adenocarcinoma

This case corresponds to a tumor estimated to be 2–3 cm in diameter and located around 4–5 o'clock by palpation within a breast of 7.7 cm diameter. The tumor was found to be an adenocarcinoma by biopsy.

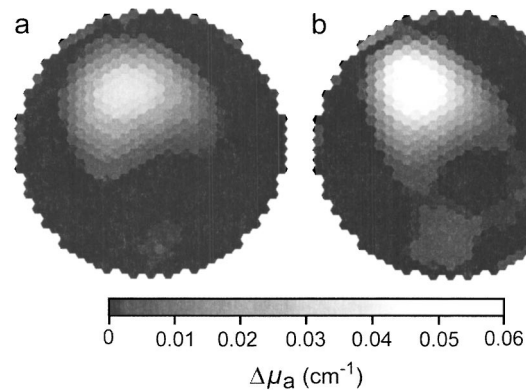


FIG. 4. Model experiment. The medium was a 10 cm diameter cylindrical tank containing a 2 cm diameter cylindrical heterogeneity. The optical parameters of the background were fixed to $\mu_a = 0.04 \text{ cm}^{-1}$ and $\mu'_s = 8 \text{ cm}^{-1}$. The contrast of the inhomogeneity was doubled from (a) $\Delta\mu_a = 0.03 \text{ cm}^{-1}$ to (b) $\Delta\mu_a = 0.06 \text{ cm}^{-1}$.

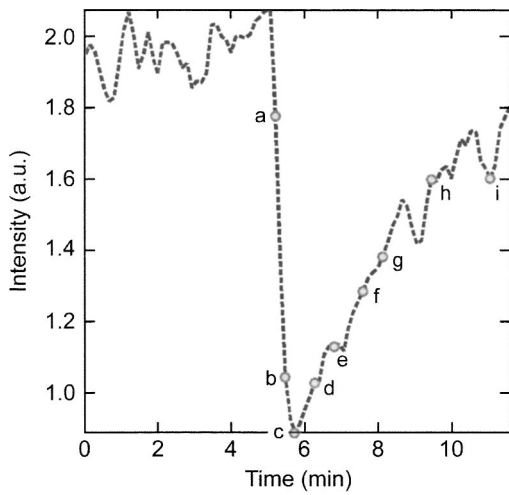


FIG. 5. The dashed curve represents the intensity drop associated to the ICG-uptake for source 14 and detector 4 (not capturing mass area) and from all data and the dots represent the selected time employed for display in Fig. 6.

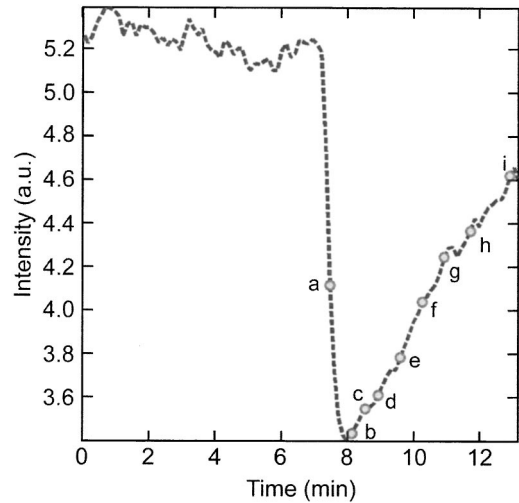


FIG. 7. The dashed curve represents the intensity drop associated to the ICG-uptake for source 2 and detector 13 (not capturing mass area) and from all data and the dots represent the selected time employed for display in Fig. 8.

An example of intensity trace collected by one detector for a particular source is displayed in Fig. 7 (source 2 and detector 13). The differential absorption reconstructions using the selected time represented by dots in Fig. 7 are presented in Fig. 8.

The reconstructions exhibit a maximum of uptake at 4 o'clock and for $\Delta\mu_a = 0.025 \text{ cm}^{-1}$, 2 cm deep in the breast. The half-width maximum value for the maximum reconstructed object is $2.5 \text{ cm} \times 2 \text{ cm}$.

3. Case III: Invasive ductal carcinoma

This patient had a cancer in the lower quadrant of the breast, and its size was estimated to be $4 \text{ cm} \times 3 \text{ cm}$. The maximum differential absorption observed was $\Delta\mu_a$

$= 0.042 \text{ cm}^{-1}$. The position of the tumor was easily estimated from the surface as long as the skin surface was rough like a "peau d'orange" (orange skin—malignant obstruction of the superficial lymphatic channels) at 6 o'clock. The tumor was found to be an invasive ductal carcinoma by biopsy.

An example of the intensity trace collected by one detector for a particular source is displayed in Fig. 9 (source 6 and detector 3). The differential absorption reconstructions, using the selected time represented by dots in Fig. 9, are presented in Fig. 10.

The reconstructions exhibit a maximum of uptake at 6 o'clock, 2 cm deep from the breast surface. This location corresponds to the expected location of the tumor. The half-

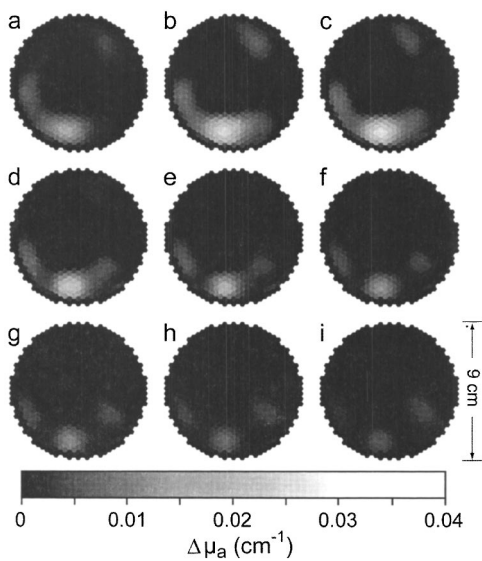


FIG. 6. Differential absorption reconstructions for the time selected in Fig. 5. The frames are normalized to the same colorbar. The reconstructions are arranged in rows corresponding to the time course.

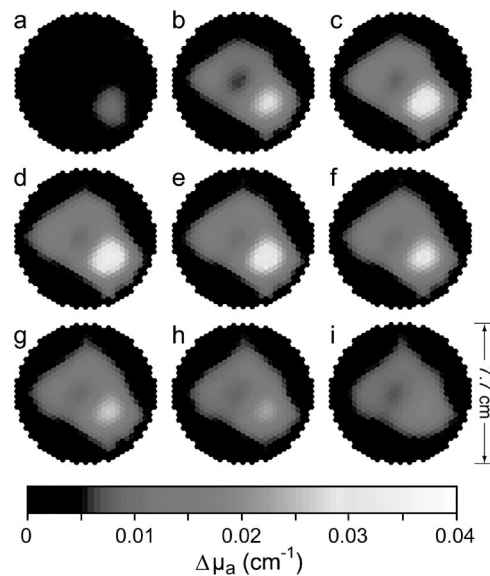


FIG. 8. Differential absorption reconstruction for the time selected in Fig. 7. The frames are normalized to the same colorbar. The reconstructions are arranged in rows corresponding to the time course.

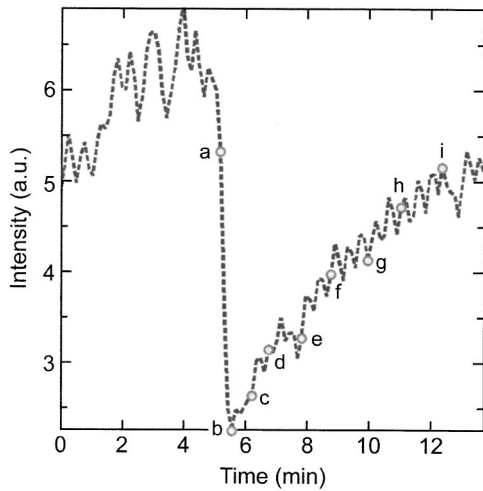


FIG. 9. The dashed curve represents the intensity drop associated to the ICG-uptake for source 6 and detector 3 (not capturing mass area) and from all data and the dots represent the selected time employed for display in Fig. 10.

width maximum value for the maximum reconstructed object is 3.5 cm×3 cm.

4. Pharmacokinetics

From the differential absorption, we can trace the ICG-uptake locally in the tumor area as the ICG related absorption is linearly associated to the dye concentration. Figure 11 depicts the pharmacokinetics of the voxel exhibiting the maximum uptake in the tumor area for the three cases investigated herein.

The origin of time was chosen to be the first rising point in the pharmacokinetics. The data were obtained from the reconstructions at the sampling rate of the apparatus (8.8 s).

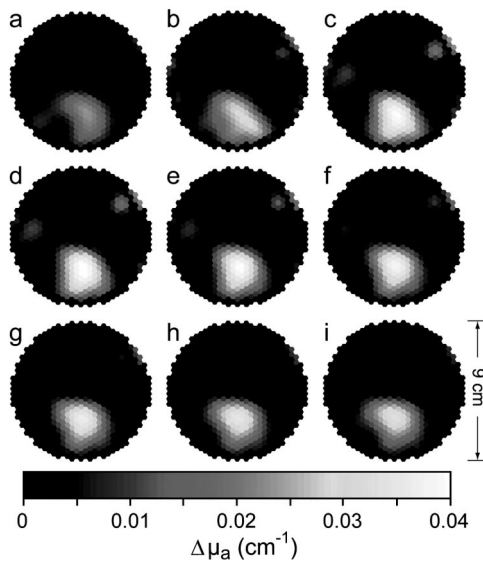


FIG. 10. Differential absorption reconstruction for the time selected in Fig. 9. The frames are normalized to the same colorbar. The reconstructions are arranged in rows corresponding to the time course.

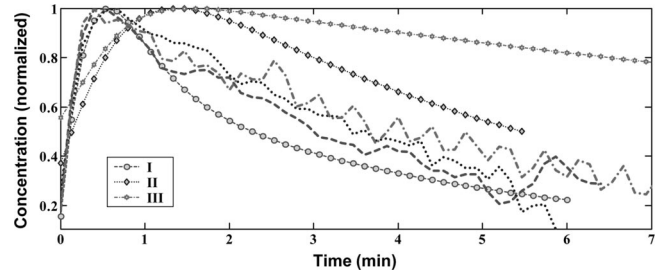


FIG. 11. Time course for the voxel exhibiting the maximum uptake in the suspicious area (curves with geometrical markers) and for healthy tissue (curves without geometrical markers). The uptakes are normalized to their maximum.

For conciseness we do not show the entire set of reconstructions. The pharmacokinetics uptakes are normalized to their respective maximum.

In Table I, the pharmacokinetics constants for healthy tissue and tumoral tissue are presented. The tumor tissues correspond to the voxel exhibiting the maximum of ICG uptake in the tomographic reconstructions, while the healthy tissue correspond to the pharmacokinetics of a projection not capturing the tumor area.

For case I, the ICG uptake was rapid both for the healthy tissue and the presumed tumor area. No wash-in, wash-out rate differences was observable for this case.

Case II exhibited differences only in the wash-in rate. The tumor expressed a slower uptake rate. The wash-out times were identical for healthy and diseased tissue.

Finally, case III exhibited uptake difference for both rates. The diseased tissue demonstrated a slower uptake and slow washout rate.

IV. DISCUSSION

A. Physiological significance

In all the three cases presented herein, the suspicious areas were well localized using DOT. In each case, a differential uptake was observed in the area expected from palpation. Moreover, the estimated size of the mass from the FWHM of the maximum peak uptake was close to that estimated by palpation. This result underlines the ability of contrast-enhanced CW DOT to perform accurate localization and delineation of the tumor *in vivo*.²⁸ The net differential uptake,

TABLE I. Rate constant of ICG uptake and excretion for diseased and healthy tissue.

	Case					
	I		II		III	
	Healthy	Tumor	Healthy	Tumor	Healthy	Tumor
α (min ⁻¹)	3.13	3.23	1.97	1.43	2.59	1.61
β (min ⁻¹)	0.17	0.19	0.21	0.20	0.20	0.05
$\alpha + \beta$	3.30	3.42	2.18	1.63	2.79	1.66
R^2	0.99	0.98	0.98	0.99	0.97	0.99

as estimated in this study, is associated with an increase of the density of the capillary bed (angiogenesis).

Additionally, discrimination between healthy and diseased tissue was observed in the pharmacokinetics of ICG. The pharmacokinetics were similar only for case I. In the two other cases, the tumor area exhibited a slower uptake and slower release of the contrast agent. This finding is remarkable because ICG is normally considered to be a blood persistent contrast agent that is not expected to have preferential uptake in diseased tissue.⁴⁴ Discrepancies in uptake/excretion rate could be attributed to the leakiness of the blood wall of the contrast agent if extravasation is not ruled out.¹⁷

In solid tumors, microvessels exhibit a series of severe structural and functional abnormalities (abnormal vessel wall, abnormal vascular architecture and abnormal vascular density).⁴⁵ Excessive branching is a common finding often coinciding with blind vascular endings. This chaotic vascular organization is responsible for an increase in geometric resistance to flow.⁴⁶ Moreover, there is an increased vascular permeability leading to a rise in local viscous resistance to blood flow.

Near-infrared techniques are sensitive to the local average blood flow due to their low resolution. Furthermore, they are more sensitive to the microvessels than the large vessels, especially in the case of contrast agent.⁴⁷ We believe our observations reflect the sensitivity of the technique to resistance of small poorly perfused vessels and to the extravasation of the molecule.

B. Limitations

However, we have to underline the limitations of our study. Our data-set was collected in the CW mode. Thus, an accurate estimation of the average optical properties of the postinjection scan used as a baseline for all the reconstructions herein was not possible. Therefore, our forward model was calculated with the average properties of breast tissue at this wavelength reported in the literature.⁴⁸ These average optical properties can be patient and status hormonal dependent.^{7,8} Thus, in our reconstructions, a mismatch between the forward model and the *in vivo* optical scattering properties is likely to be present. This mismatch affects the quality and the quantitative estimate of the object function.⁴⁹ For instance, in case II, the overall background reconstruction could be attributed to a mismatch in the optical background properties of the forward model which probably affect the wash-out rate estimated in the tumor area. These effects, however, are less important in the case of a Rytov formulation than in a case of a Born one.⁵⁰ Furthermore, the scheme employed in this study is based on a full differential approach ($\Phi_{sc}(\vec{r}_s, \vec{r}_d) = -\ln[U_{\text{post-injection}}(\vec{r}_s, \vec{r}_d)/U_{\text{pre-injection}}(\vec{r}_s, \vec{r}_d)]$). As demonstrated by Ntziachristos *et al.*,³⁷ a full differential approach is less sensitive to a background mismatch, especially for detectors on the opposite side of the breast from the source.

Finally we used the coupling coefficient technique to attenuate the effect of biological noise such as breathing arti-

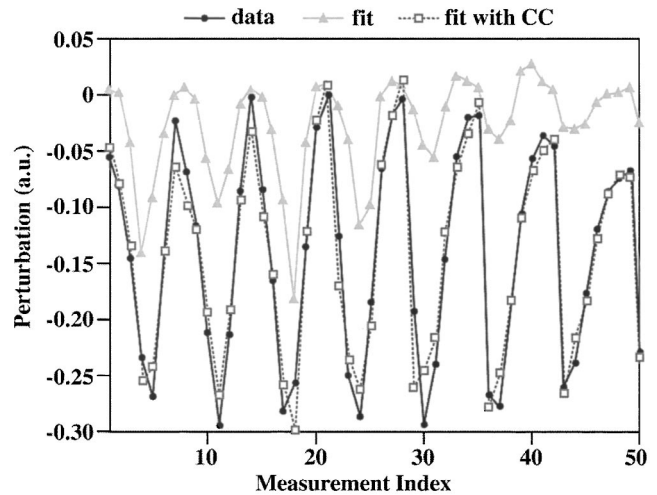


Fig. 12. Measurement vector and fitting vector with and without coupling coefficient ($\Phi_{sc}(\vec{r}_s, \vec{r}_d) = -\ln[U_{\text{post-injection}}(\vec{r}_s, \vec{r}_d)/U_{\text{pre-injection}}(\vec{r}_s, \vec{r}_d)]$).

facts. An example of the best fit obtained for an inversion with and without the coupling coefficient is provided in Fig. 12. Whereas this technique has been devised to obtain a robust calibration method, it is still necessary to employ it in our approach as the source/detector-tissue coupling could be modified during the time course of the experiment. These modifications could occur simply on a subset of optodes and then lead to significant reconstruction artifacts. Including the source strength and detector gain as unknowns in the inverse problems enables us to diminish the impact of coupling noise.

Noticing these two facts, we did not stress the quantitative aspect of the uptake (maximum concentration). This parameter could be plagued by uncertainties linked to our linear approach. However, in the case of full differential scheme demonstrated by Y. Pei *et al.*,⁵¹ the relative time reconstructions are not much affected by the reference optical properties mismatch.

Due to these methodological uncertainties, the preliminary hypothesis of Sec. IV A should be confirmed in future studies.

V. CONCLUSIONS AND PERSPECTIVES

In this article we reported diffuse optical tomographic imaging of ICG uptake by breast suspicious mass *in vivo*. In all three cases investigated herein, clear localization of the suspicious area was achieved, correlated well with *a priori* information obtained by palpation. Moreover, different pharmacokinetics were found between healthy and diseased tissue in the two malignant cases. This finding is possibly related to the morphological differences in the vascularization between healthy and diseased tissues. This accumulation of ICG in tumor is a nonspecific,⁵² transient³⁰ mechanism. It is related to the degree of angiogenesis of the suspicious mass. These results suggest that local *in vivo* ICG pharmacokinetics in breast tumors have the potential to be used as a diagnostic tool for improvement of the specificity of the optical techniques.

More cases are necessary for these studies to reach statistical relevance. Improvements in the apparatus and in the reconstruction algorithm are under development. A new apparatus with better signal-to-noise ratio and faster scan speeds is under development.⁵³ Thus we expect to make a more precise measurement of the slow component of the double compartment model. Finally, an improved implementation of the algorithm with breast shape boundary conditions is underway.

ACKNOWLEDGMENTS

The authors are grateful to Mary Leonard for excellent drafting and Dorothea Coleman for text revisions. The authors wish to thank Sam Achilefu for relevant discussions. This work was supported in part by the National Institute of Health Grant No. CA 87046. AGY acknowledges partial support from NIH Grant No. CA R01-CA 60182-05.

^aElectronic mail: intes@mail.med.upenn.edu

¹T. McBride, B. Pogue, S. Jiang, U. Osterberg, and K. Paulsen, "Initial studies of *in-vivo* absorbing and scattering heterogeneity in near-infrared tomographic breast imaging," *Opt. Lett.* **26**, 822–824 (2001).

²H. Jiang, N. Iftimia, J. Eggert, L. Fajardo, and K. Klove, "Near-infrared optical imaging of the breast with model-based reconstruction," *Acad. Radiol.* **9**, 186–194 (2002).

³M. Franceschini, K. Moesta, S. Fantini, G. Gaida, E. Gratton, H. Jess, W. Mantulin, M. Seeber, P. Schlag, and M. Kaschke, "Frequency-domain techniques enhance optical mammography: Initial clinical results," *Proc. Natl. Acad. Sci. U.S.A.* **94**, 6468–6473 (1997).

⁴S. Colak, M. van der Mark, G. Hooft, J. Hoogenraad, E. van der Linden, and F. Kuijpers, "Clinical optical tomography and NIR spectroscopy for breast cancer detection," *IEEE J. Sel. Top. Quantum Electron.* **5**, 1143–1158 (1999).

⁵M. Holboke, B. Tromberg, X. Li, N. Shah, J. Fishkin, D. Kidney, J. Butler, B. Chance, and A. Yogh, "Three dimensional diffuse optical mammography with ultrasound localization in a human subject," *J. Biomed. Opt.* **5**, 237–247 (2000).

⁶A. Cerussi, A. Berger, F. Bevilacqua, N. Shah, D. Jakubowski, J. Butler, R. Holcombe, and B. Tromberg, "Source of absorption and scattering contrast for Near-Infrared optical mammography," *Acad. Radiol.* **8**, 211–218 (2001).

⁷B. Chance, "Near-infrared optical spectroscopy characterizes breast tissue hormonal and age status," *Acad. Radiol.* **8**, 209–210 (2001).

⁸N. Shah, A. Cerussi, C. Eker, J. Espinoza, J. Butler, J. Fishkin, R. Hornung, and B. Tromberg, "Noninvasive functional optical spectroscopy of human breast tissue," *Proc. Natl. Acad. Sci. U.S.A.* **98**, 4420–4425 (2001).

⁹T. Troy, D. Page, and E. Sevick-Muraca, "Optical properties of normal and diseased breast tissues: prognosis for optical mammography," *J. Biomed. Opt.* **1**, 342–355 (1996).

¹⁰B. Ebert, U. Sukowski, D. Grosenick, H. Wabnitz, K. Moesta, K. Licha, Q. Becker, W. Semmler, P. Schlag, and H. Rinnerberg, "Near-infrared fluorescent dyes for enhanced contrast in optical mammography: phantom experiments," *J. Biomed. Opt.* **6**, 134–140 (2001).

¹¹G. Trecate, J. Tess, D. Vergnaghi, S. Bergonzi, G. Mariani, C. Ferraris, and R. Musumeci, "Lobular breast cancer: How useful is breast magnetic resonance imaging?" *Tumori* **87**, 232–238 (2001).

¹²E. Bombardieri and F. Crippa, "PET imaging in breast cancer," *Q. J. Nucl. Med.* **45**, 245–256 (2001).

¹³D. Hawryls and E. Sevick-Muraca, "Developments toward diagnostic breast cancer imaging using Near-Infrared optical measurements and fluorescent contrast agents," *Neoplasia* **2**, 388–417 (2000).

¹⁴V. Ntziachristos and B. Chance, "Probing physiology and molecular function using optical imaging: applications to breast cancer," *Breast Cancer Res.* **3**, 41–47 (2001).

¹⁵R. Weissleder and U. Mahmood, "Molecular imaging," *Radiology* **219**, 316–333 (2001).

¹⁶R. Weissleder, C. H. Tung, U. Mahmood, and A. Bogdanov, "*In vivo* imaging with protease-activated near-infrared fluorescent probes," *Nat. Biotechnol.* **17**, 375–378 (1999).

¹⁷J. Bugaj, S. Achifelu, R. Dorshow, and R. Rajagopalan, "Novel fluorescent contrast agents for optical imaging of *in-vivo* tumors based on a receptor-targeted dye-peptide conjugate platform," *J. Biomed. Opt.* **6**, 122–133 (2001).

¹⁸K. Licha, B. Riefke, V. Ntziachristos, A. Becker, B. Chance, and W. Semmler, "Hydrophilic cyanine dyes as contrast agents for near-infrared tumor imaging: synthesis, photophysical properties and spectroscopic *in-vivo* characterization," *Photochem. Photobiol.* **72**, 392–398 (2000).

¹⁹R. Benson and H. Kues, "Fluorescence properties of indocyanine green as related to angiography," *Phys. Med. Biol.* **23**, 159–163 (1978).

²⁰R. Branch, J. James, and A. Read, "The clearance of antipyrine and indocyanine green in normal subjects and in patients with chronic liver disease," *Clin. Pharmacol. Ther.* **20**, 81–89 (1976).

²¹C. Niemann, T. Henthorn, T. Krejcie, C. Shanks, C. Enders-Klein, and M. Avram, "Indocyanine green kinetics characterize blood volume and flow distribution and their alteration by propranolol," *Clin. Pharmacol. Ther.* **67**, 342–350 (2000).

²²T. Desmettre, J. Devoiselle, and S. Mordon, "Fluorescent properties and metabolic features of Indocyanine Green (ICG) as related to angiography," *Surv. Ophthalmology* **45**, 15–27 (2000).

²³K. Motomura, H. Inaji, Y. Komoike, T. Kasugai, S. Nogushi, and H. Koyama, "Sentinel node biopsy guided by indocyanine green dye in breast cancer patient," *Jpn. J. Clin. Oncol.* **29**, 604–607 (1999).

²⁴M. O'Leary, D. Boas, B. Chance, and A. Yodh, "Reradiation and imaging of diffuse photon density waves using fluorescent inhomogeneities," *J. Lumin.* **60**, 281–286 (1994).

²⁵B. Ebert, U. Sukowski, D. Grosenick, H. Wabnitz, K. Moesta, K. Licha, A. Becker, W. Semmler, P. Schlag, and H. Rinnerberg, "Near-infrared fluorescent dyes for enhanced contrast in optical mammography: phantom experiments," *J. Biomed. Opt.* **6**, 134–140 (2001).

²⁶X. Li, B. Beauvoit, R. White, S. Nioka, B. Chance, and A. Yodh, "Tumor localization using fluorescence of Indocyanine green in rat models," *Proc. SPIE* **2389**, 789–797 (1995).

²⁷J. Reynolds, T. Troy, R. Mayer, A. Thompson, D. Waters, K. Cornell, P. Snyder, and E. Sevick-Muraca, "Imaging of spontaneous canine mammary tumors using fluorescent contrast agents," *Photochem. Photobiol.* **70**, 87–94 (1999).

²⁸S. Nioka, Y. Yung, M. Schnell, S. Zhao, S. Orel, C. Xie, B. Chance, and S. Solin, "Optical imaging of breast tumor by means of continuous waves," *Adv. Exp. Med. Biol.* **411**, 227–232 (1997).

²⁹V. Ntziachristos, A. Yodh, M. Schnell, and B. Chance, "Concurrent MRI and diffuse optical tomography of breast after indocyanine green enhancement," *Proc. Natl. Acad. Sci. U.S.A.* **97**, 2767–2772 (2000).

³⁰S. Achilefu, R. Dorshow, J. Bugaj, and R. Rajagopalan, "Novel receptor-targeted fluorescent contrast agents for *in-vivo* tumor imaging," *Invest. Radiol.* **35**, 479–485 (2000).

³¹D. Hansen, A. Spence, T. Carski, and M. Berger, "Indocyanine green (ICG) staining and demarcation of tumor margins in a rat glioma model," *Surg. Neurol.* **40**, 451–456 (1993).

³²H. Shinohara, A. Tanaka, T. Kitai, N. Yanabu, T. Inomoto, S. Satoh, E. Hatano, Y. Yamaoka, and K. Hirao, "Direct measurement of hepatic Indocyanine Green clearance with near-infrared spectroscopy: separate evaluation of uptake and removal," *Hepatology* **23**, 137–144 (1996).

³³A. ElDeosky, A. Seifalian, M. Cope, D. Delpy, and B. Davidson, "Experimental study of liver dysfunction evaluated by direct Indocyanine green clearance using near infrared spectroscopy," *Br. J. Surg.* **86**, 1005–1011 (1999).

³⁴J. A. Nelder and R. Mead, "A simplex method for function minimization," *Comput. J. (UK)* **7**, 308–313 (1965).

³⁵A. Yodh and B. Chance, "Spectroscopy and imaging with diffusing light," *Phys. Today* **48**(3), 34–40 (1995).

³⁶M. O'Leary, "Imaging with diffuse photon density waves," Ph.D. thesis, University of Pennsylvania, 1996.

³⁷V. Ntziachristos, B. Chance, and A. Yodh, "Differential diffuse optical tomography," *Opt. Express* **5**, 230–242 (1999) (<http://www.opticsexpress.org/abstract.cfm?URI=OPEX-5-10-230>).

³⁸J. Ripoll, V. Ntziachristos, R. Carminati, and M. Nieto-Vesperinas, "Kirchhoff approximation for diffusive waves," *Phys. Rev. E* **64**, 051917 (2001).

³⁹J. Ripoll, V. Ntziachristos, J. P. Culver, D. N. Pattanayak, A. G. Yodh, and

- M. Nieto-Vesperinas, "Recovery of optical parameters in multiple-layered diffusive media: theory and experiments," *J. Opt. Soc. Am. A* **18**, 821–830 (2001).
- ⁴⁰D. Boas, T. Gaudette, and S. Arridge, "Simultaneous imaging and optode calibration with diffuse optical tomography," *Opt. Express* **8**, 263–270 (2001) (<http://www.opticsexpress.org/abstract.cfm?URI=OPEX-8-5-263>).
- ⁴¹S. Arridge, "Optical tomography in medical imaging," *Inverse Probl.* **15**, R41–R93 (1999).
- ⁴²P. Hansen, "Analysis of discrete ill-posed problems by means of the L-curve," *SIAM Rev.* **34**, 561–580 (1992).
- ⁴³P. Hansen and D. O'Leary, "The use of the L-curve in the regularization of discrete ill-posed problems," *SIAM J. Sci. Comput. (USA)* **14**, 1487–1503 (1993).
- ⁴⁴M. Gurfinkel, A. Thompson, W. Ralston, T. Troy, A. Moore, T. More, J. Gust, D. Tatman, J. Reynolds, B. Mugenberg, K. Nikula, R. Pandey, R. Mayer, D. Hawrysz, and E. Sevick-Muraca, "Pharmacokinetics of ICG and HPPH-car for the detection of normal and tumor tissue using fluorescence, near infrared reflectance imaging: a case study," *Photochem. Photobiol.* **72**, 94–102 (2000).
- ⁴⁵P. Vaupel, "The influence of tumor blood flow and microenvironmental factors on the efficacy of radiation, drugs and localized hyperthermia," *Klin. Padiatr.* **209**, 243–249 (1997).
- ⁴⁶M. Suzuki, K. Hori, I. Abe, S. Saito, and H. Sato, "Functional characterization of the microcirculation in tumors," *Cancer Metastasis Rev.* **3**, 115–126 (1984).
- ⁴⁷B. Pogue, E. White, U. Osterberg, and K. Paulsen, "Absorbance of opaque microstructures in optically diffuse media," *Appl. Opt.* **40**, 4616–4621 (2001).
- ⁴⁸T. Durduran, R. Choe, J. Culver, L. Zubkov, M. Holboke, J. Giammarco, B. Chance, and A. G. Yodh, "Bulk optical properties of healthy female breast tissue," *Phys. Med. Biol.* **47**, 2847–2861 (2002).
- ⁴⁹X. Cheng and D. Boas, "Systematic diffuse optical image errors resulting from uncertainty in the background optical properties," *Opt. Express* **4**, 299–307 (1999) (<http://www.opticsexpress.org/abstract.cfm?URI=OPEX-4-8-299>).
- ⁵⁰M. O'Leary, D. Boas, B. Chance, and A. Yodh, "Simultaneous scattering and absorption images of heterogeneous media using diffusive waves within the Rytov approximation," *Proc. SPIE* **2389**, 320–327 (1995).
- ⁵¹Y. Pei, H. Graber, and R. Barbour, "Influence of systematic errors in reference states on image quality and on stability of derived information for dc optical imaging," *Appl. Opt.* **40**, 5755–5769 (2001).
- ⁵²X. Li, B. Beauvoit, R. White, S. Nioka, B. Chance, and A. Yodh, "Tumor localization using fluorescence of Indocyanine Green (ICG) in rat models," *Proc. SPIE* **2389**, 789–797 (1995).
- ⁵³Y. Lin, G. Lech, S. Nioka, X. Intes, and B. Chance, "Non-invasive, low-noise, fast imaging of blood volume and deoxygenation changes in muscles using LED continuous-wave imager," *Rev. Sci. Instrum.* **73**, 3065–3074 (2002).